THE JOURNAL OF PHYSICAL CHEMISTRY B LETTERS

2007, *111,* 8708−8712
Published on Web 07/06/2007

Surfactant Aggregates at Rough Solid−Liquid Interfaces

Hannes C. Schniepp, Ho C. Shum,† Dudley A. Saville,‡ and Ilhan A. Aksay*

Department of Chemical Engineering, Princeton University, Princeton, New Jersey 08544-5263

Received: May 6, 2007; In Final Form: June 10, 2007

We demonstrate improved atomic force microscopic imaging of surfactant surface aggregates, featuring an increase in the topography contrast by several hundred percent with respect to all previous studies. Surfactant aggregates on rough gold surfaces, which could not be imaged previously because of low resolution, display substantially different morphologies when compared with atomically smooth materials.

Introduction

The adsorption of surfactants at interfaces is important for many technical applications and industrial processes such as detergency, froth flotation,[1] boundary lubrication,[2−4] colloid stabilization,[5,6] dispersion,[7] and corrosion inhibition.[8,9] Interactions of surfactants with metallic surfaces have become important in the production of nanoparticles.[10−12] Traditionally, the adsorption behavior of surfactants has been studied by depletion methods[13−18] and streaming potential techniques.[16,19] More recently, experimental efforts applying ellipsometry,[20−22] optical reflectometry,[23,24] electrochemical methods,[9] quartz crystal microbalances,[25] and Fourier transform infrared spectroscopy[26] have added information about the dynamic properties of surfactant adsorption. Fluorescence decay,[27] neutron reflection,[28] and grazing-incidence small-angle neutron scattering techniques[29] have provided general information about the length scales of the surface aggregates, and microcalorimetry[30−34] has been used to determine the corresponding heats of adsorption. None of these techniques, however, provide high enough spatial resolution to visualize surfactant adsorption at the molecular level.

The best approach so far to obtain detailed morphological information on surface aggregates at the nanometer level has been to use liquid-cell atomic force microscopy (AFM).[35,36] Pioneered by Manne and co-workers, this technique revealed that surfactants form surface aggregates in the shape of full[36] or half [35−38] cylinders or full[36] or half [39] spheres, as well as flat layers,[36,40] depending on the system under investigation. These findings have been confirmed by computational investigations.[41] AFM imaging of surfactant surface micelles, however, has been limited to extremely flat substrates such as atomically smooth graphite[35−37,42−45] and mica.[36,40,42] Amorphous silica that forms as a native oxide on highly smooth silicon has been the third most popular substrate.[5,36,46]

We are interested in rough surfaces that are present in most engineering applications. There have been speculations[47,48] that even very small deviations from an atomically smooth surface quality (16 pm root-mean-square roughness in a 50 nm × 50 nm area)[49] have a direct influence on surfactant adsorption. In order to be able to image surfactant aggregates on rough surfaces, we use recently developed, soft AFM cantilevers with very sharp tips. Artifacts due to the size and shape of the tip that previously prevented micellar resolution on rough surfaces are hence greatly reduced. Using these probes, we investigate aggregates of sodium dodecyl sulfate (SDS) surfactant on gold surfaces. Gold substrates can be rendered rough or atomically flat, thus enabling us to compare the role of surface roughness while keeping all other parameters fixed.

Experimental Section

Preparation of Samples and Solutions. We prepared our samples by evaporating a 100 nm thick gold film directly onto unheated, freshly cleaved mica substrates. This was accomplished using a Denton V-502A (Denton Vacuum, Moorestown, NJ) electron beam evaporator at pressures below 10^{-6} mbar and an evaporation rate of 0.3 nm/s. The samples were either used with the rough surface obtained after this step[50] or treated further to render the surfaces as smooth as possible. This was achieved by annealing with a hydrogen flame, using a National 3H stainless steel hydrogen torch with an OX-3 tip (Premier Industries, Blaine, MN). The hydrogen pressure was 400 mbar, and the torch regulator was adjusted to yield a flame about 7 cm long. The mica sheets were held in the flame for about 10 s at a distance of about 5 cm from the torch tip. For both the rough and the annealed gold films, we confirmed that the (111) planes were oriented parallel to the substrate surface by X-ray diffraction characterization and atomic resolution AFM lattice scans, respectively. The annealed samples were used within minutes after the annealing process to reduce contamination from air as much as possible.

The surfactant solutions were prepared from solid SDS (BioChemika Ultra, grade ≥ 99% (GC), Fluka, Buchs, Switzerland) and water with a resistivity of 18 MΩ cm, deionized with a Picopure 2 UV Plus system (Hydro Service and Supplies, Inc., Durham, NC). The SDS solutions were always prepared fresh and used within a few hours in order to avoid the formation of dodecanol via hydrolysis.[51,52] The pH value of the surfactant solutions was not further adjusted.

* Corresponding author.
† Currently at Engineering Sciences Laboratory, Harvard University, Cambridge, Massachusetts 02138.
‡ Deceased, October 4, 2006.

10.1021/jp073450n CCC: $37.00

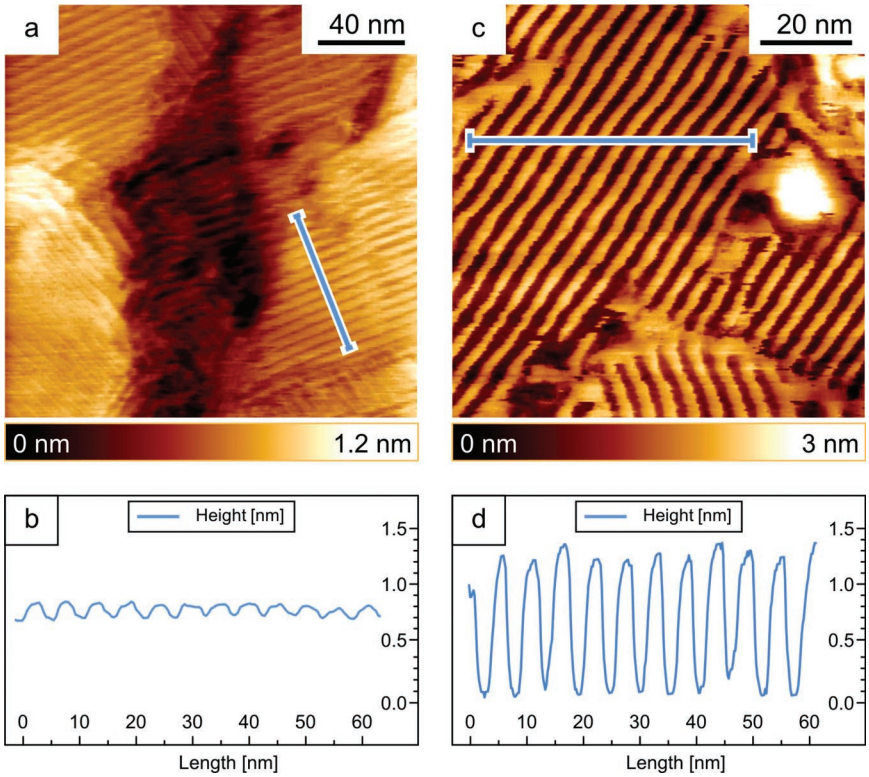

Figure 1. (a) 200 × 200 nm AFM scan of SDS aggregates on top of an annealed gold(111) film using a silicon nitride tip (SDS concentration: 10 mM). The gold surface is not perfectly flat but features several topography steps. (b) Cross section along the blue line in panel a. (c) 90 × 90 nm AFM scan of a flame-annealed gold surface immersed in a 10 mM SDS solution, using sharp silicon tips. (d) Cross section along the blue line in panel b.

Atomic Force Microscopy. The images were acquired using a commercial MultiMode AFM (Veeco, Santa Barbara, CA) with a NanoScope IIIa controller (software version v5.12r5), equipped with an FC type contact-mode liquid cell. The AFM piezo scanner was calibrated using a 3D reference silicon grating (Veeco, part number 498-000-026) with a 10 μm lateral pitch and a step height of 100 nm. Two types of cantilevers were applied: (i) NP−S type (Veeco) oxide-sharpened silicon nitride tips with a reflective gold coating on the back side and a nominal spring constant and tip radius of curvature of 0.06 N/m and 20 nm, respectively and (ii) PointProbe Plus PPP−BSI (Nanosensors, Neuchatel, Switzerland) highly doped silicon cantilevers with tip radii below 7 nm and a nominal spring constant of 0.05 N/m without reflective coatings. All tips were cleaned in an ozone chamber (UVOCS, Montgomeryville, PA) for 60 min prior to the experiment. The fluid cell (volume: 0.5 mL) was flushed with 5 mL of surfactant solution before the experiment was started. All images were taken at line frequencies of 2−7 Hz and the highest possible integral and proportional gains (typically ~5) to achieve imaging at the lowest possible forces and to get the most accurate representation of the sample. For imaging the micellar aggregates, the sample was approached with the smallest possible force set point. Once the tip was within a few nanometers of the surface, the force set point was optimized for best contrast.

Results and Discussion

Atomically Smooth Gold Surfaces. A topography image of surface micelles on a flame-annealed gold surface in an aqueous 10 mM SDS solution (just above the SDS critical micelle concentration of 8.1 mM)[15,53] obtained with a silicon nitride (NP−S) tip is shown in Figure 1a. The large areas of different color, dark in the center, brighter on the left and right sides, represent atomically smooth terraces of the annealed gold sample. All of these terraces are covered by close-packed, hemicylindrical micelles with a constant spacing of about 5.1 nm, represented by the periodic topography modulations in the shape of lines.[54,55] Figure 1b features a cross section following the blue line in Figure 1a showing that the topography modulation induced by the micellar aggregates is 0.1−0.2 nm. The vertical spacing between the hexagonal layers of gold that form the terraces is known to be 0.235 nm,[56] suggesting that the topography steps between the terraces in Figure 1a are one to four atomic layers high.

When we image the same system with one of the sharper silicon (PPP−BSi) tips, a much higher contrast is achieved as shown in the topography image and the corresponding cross section in Figure 1c,d, respectively. The topography modulation induced by the micellar surface aggregates is now on the order of as much as 1.2 nm. This represents an improvement of about 1,000% in modulation with respect to what we typically get with silicon nitride tips. The image now displays the surfactant aggregates in much greater detail.

Rough Gold Surfaces. Images acquired with a Si_3N_4 tip on rough gold surfaces are shown in Figure 2. For a reference characterization of the surface, Figure 2a was taken in deionized water only. The image shows the grainy gold surface with grain diameters of 30−100 nm.[56] The grains are typically 3−7 nm high. If surfactant is added to the solution (10 mM SDS), the AFM image (Figure 2b) only shows very subtle changes. If directly compared with Figure 2a, small ripples on the grains can be observed. At this point, one can only suspect that these ripples indicate the presence of surface micelles. It is, however, impossible to identify individual micelles or even recognize their shapes.

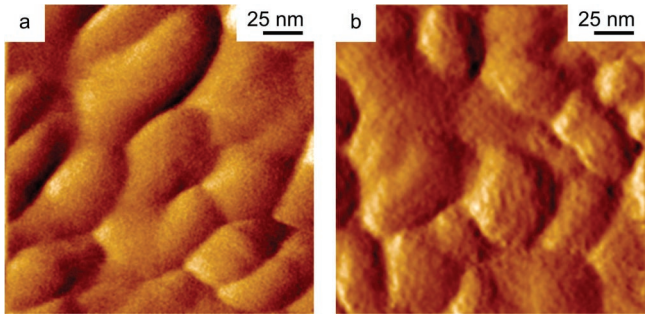

Figure 2. AFM deflection images acquired with a standard silicon nitride tip taken on a rough gold surface immersed in (a) water only and (b) a 10 mM SDS solution.

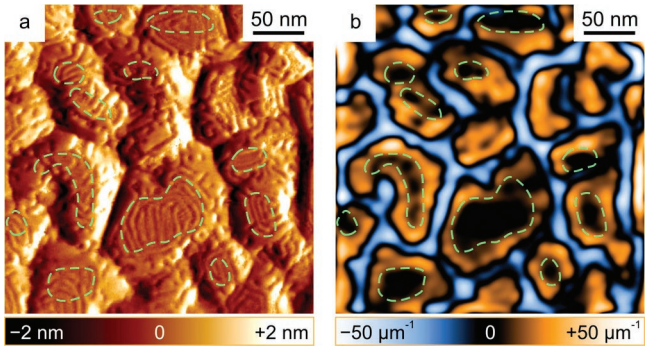

Figure 3. (a) AFM deflection image of surfactant aggregates on a rough gold film in contact with a 10 mM SDS solution taken with a sharp silicon AFM tip. (b) Calculated mean curvature of the surface shown in panel a. Larger areas with low curvature (dark color) on top of the grains are highlighted by green, dashed lines. The same lines are shown in panel a to illustrate the correlation between low substrate curvature and elongated micelle morphology.

In contrast, applying the sharp PPP−BSi tips to image surfactant aggregates on rough surfaces, we achieved a breakthrough. As the deflection image in a 10 mM SDS solution (Figure 3a) shows, the entire gold surface is indeed covered with micellar surface aggregates. The geometry of each surface micelle is clearly revealed: The micelles are wormlike, featuring similar diameters of 5−9 nm, but with a large variety of lengths. In comparison to the AFM images acquired on smooth gold (Figure 1c), the micelles on rough gold surfaces display very different micelle morphologies (Figure 3a). The micelles on smooth gold are very long, parallel, and equidistant, in agreement with previously reported results,[55] where their orientation has been shown to be dictated by the gold lattice. On rough gold, in contrast, they are quite curved and exhibit a considerable range of lengths. The shortest ones are of almost hemispherical shape; the larger ones are more than 50 nm in length. We observe that the longer micelles on top of larger grains display a rather flat topography, while the shorter ones are located on small grains that are curved more strongly. A definitive relation to the gold lattice structure is not yet established.

To analyze these images more quantitatively, we computed a color-coded surface curvature map (Figure 3b) of the area shown in Figure 3a. We first applied a low-pass filter to the corresponding topography data to suppress features of micellar size or smaller; then, we calculated the mean curvature[57] κ at each point. The peak values correspond to radii of curvature $R = 1/\kappa$ of ± 20 nm, where we use negative numbers and blue colors for concave areas (such as in the grooves between the grains) and positive numbers and ochre colors for convex areas (typically on the sides of the grains). The analysis confirms our observation expressed above: the larger areas of low curvature

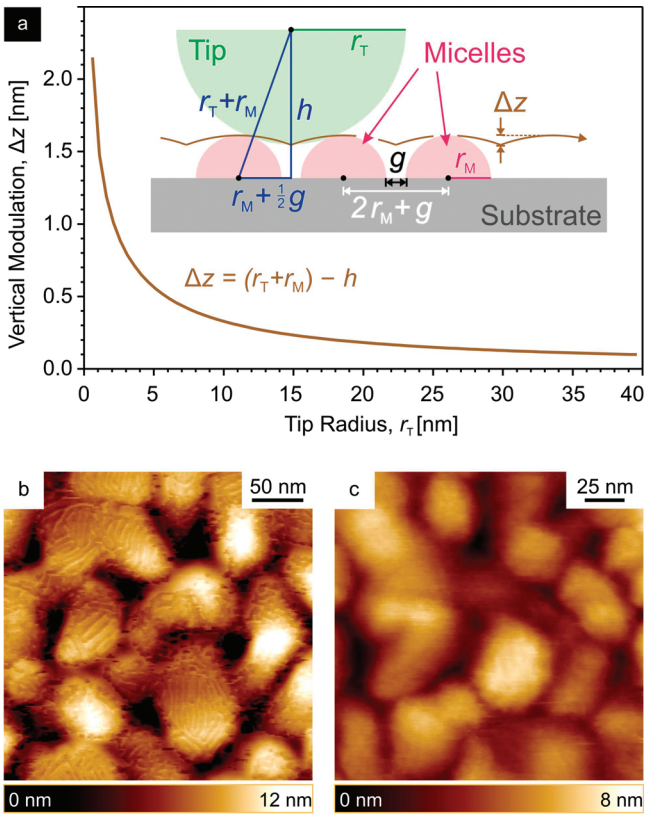

Figure 4. (a) When the AFM tip (idealized by a sphere of radius r_T) is larger than the imaged micelles (idealized by hemicylinders of radius r_M and with an intermittent gap of width g), the topography modulation is relatively small. By assuming that the tip is in hard contact with the sample and all bodies are incompressible, we can calculate the modulation Δz as a function of r_T, as shown in the plot ($r_M = 1.9$ nm, $g = 1.3$ nm). (b) Topography image of an evaporated gold film in a 10 mM SDS solution taken with a sharp AFM probe, featuring a high topography contrast. (c) When a Si_3Ni_4 tip is applied on a similar sample, the topography contrast is extremely weak.

($|\kappa| < 5\ \mu m^{-1}$) on top of the grains (dark areas, highlighted by green, dashed lines) generally correlate with the areas that accommodate elongated micelles, while the brighter, ochre and blue areas typically host shorter or odd-shaped aggregates. One possible explanation for this behavior is that bending elongated micelles is energetically less favorable than forming several shorter micelles that are bent to a lesser degree. This is in line with the fact that we do not observe any micelles spanning two or more grains, which would also require a significant amount of bending due to the sample topography.

Importance of the AFM Probe Size. The aggregates of many commonly studied surfactants on smooth surfaces are close-packed micelles of cylindrical, hemicylindrical, or spherical shape with typical center-to-center distances of 5−7 nm.[36] We aim to estimate the influence of the size of the AFM probe on the obtained image of such samples, which proves relatively difficult. The micellar aggregates are soft structures that are removed from the surface by energies as little as 10−20 kJ/mol.[33] The interactions between the tip and the sample are very complex and include electrostatic repulsion,[58] van der Waals attraction, hydrophobic interactions, and steric forces.[59] Furthermore, the manufacturing process of AFM probes[60] is subject to fluctuations, making their exact geometries at the nanometer scale unknown.

We use a much simplified, geometric model for our estimate, as illustrated in Figure 4a. We idealize the tip by a sphere of radius r_T; the micelles are simplified by identical hemicylinders

or hemispheres of radius r_M placed on a perfectly flat substrate. Further, we consider a gap of width g between the micelles[38,45,55] due to electrostatic repulsion between the head groups of the ionic surfactants. We assume that the tip and the micelles are incompressible and that the tip is in hard contact with the micelles while imaging. Consequently, the tip follows the wiggled, brown line in Figure 4a, featuring a vertical modulation Δz as it slides across the micelle-covered surface. We further estimate the micelle radius r_M to be equal to the length of a fully stretched SDS molecule, $r_M = 1.9$ nm.[61] Using the measured center-to-center distance $d = 5.1$ nm between the micelles, we determine g via the relationship $g = d - 2r_M = 1.3$ nm, a value that is backed by experimental evidence.[45] On the basis of these assumptions, we computed the topography contrast Δz as a function of the tip radius r_T (brown curve in Figure 4a). We assume no population of the anionic surfactant at the AFM tips[45] which are made out of either silicon or silicon nitride (Si_3N_4). Both materials develop a negative surface charge[62] in neutral pH as they form an oxide layer at the surface, so that repulsion between tip and surfactants is expected.

For a tip radius of 15 nm, our model suggests a Δz of about 0.2 nm, slowly decreasing when the tip radius is increased (Figure 4a). For tip radii of 10 nm and less, there is a relatively steep increase of the contrast as the tip radius is decreased. In the majority of previous AFM studies of these structures, Si_3N_4 cantilevers with tip radii of 20 nm and above were used. In a few studies,[37,38] silicon probes with a tip of around 15 nm were applied. In both cases, a topography contrast of 0.1−0.2 nm was reported,[38,45,46] in good agreement with our simple model. This topography contrast is small compared with other topographic features present in most samples, caused by defects in the substrate, nonplanarity, sample tilt, and scanner bow. Even in Figure 1a where the total substrate topography consists of only a few atomic steps, the micelles are hard to recognize in some parts of the image. For this reason, practically all published images show the deflection signal instead of the topography to emphasize the visibility of the micelles.[46] The disadvantage of deflection images is that they do not allow for quantitative topography analysis and are dependent on parameters such as the scanning speed and the gain of the servo loop. Using the sharp silicon probes, we achieve a much higher contrast that allows us to directly show the topography information, avoiding the difficulties associated with the deflection images. This is demonstrated in Figure 1c where the micelles are visible in high clarity throughout the entire topography image, even though the peak-to-peak topography (3 nm) is much higher than in Figure 1a (1.2 nm). Figure 4b shows that the micelle-induced topography contrast is even high enough to visualize the surfactant aggregates in a topography image taken on a rough surface with a peak-to-peak topography of 12 nm. Our model predicts a topography contrast of about 0.6 nm for the sharp tips ($r_T = 5$ nm). This is what we see in some cases (Figure 3a); in other cases (Figures 1c and 4b), we obtain a topography contrast up to 1.2 nm. This discrepancy either is due to our oversimplified model or is because some tips are sharper than specified. According to our model, the observed topography contrast of 1.2 nm would be reached with a tip radius of about 2 nm.

Topography images of surfactant aggregates on rough surfaces taken with a Si_3N_4 tip, in contrast, are essentially useless. Figure 4c shows the topography image that corresponds to the deflection image shown in Figure 2b: the topography contrast induced by the surfactant aggregates is negligible with respect to the topography of the rough substrate; the micelles are invisible in the topography signal. To explain this weak performance, we suggest the following mechanism. When the lateral extent of the interaction zone between the tip and the surface is larger than the width of one micelle, the image is effectively averaged over two or more micelles. On a flat sample, where the micellar pattern is periodic, the image is still likely to reproduce this periodicity. On the rough surface, in contrast, where the micelles are disordered (Figure 3a), this averaging process further diminishes the micelle-induced topography contrast.

Conclusions

We improved the AFM imaging contrast of close-packed SDS surfactant surface aggregates on gold surfaces from 0.1−0.2 nm to about 1.2 nm by using silicon AFM cantilevers with very low spring constants and sharp tips. Imaging the morphology of surfactant surface aggregates on rough surfaces thus became possible for the first time. Similar to what is found on smooth surfaces, SDS surfactant aggregates on rough gold surfaces are primarily of hemicylindrical shape. More work is necessary to study the relationship between substrate structure and micelle morphology. Generally, we find that the micelle length depends strongly on the surface curvature. The less curved areas support the formation of longer, hemicylindrical micelles; in areas of higher curvature, the aggregates are shorter, approaching a hemispherical morphology.

Acknowledgment. We gratefully acknowledge the help of Michael J. Souza and Caroline M. Murira with flame annealing and providing evaporated gold samples. We thank Sebastian Kossek at Nanoscience Instruments for helpful discussions about AFM probes. Financial support from ARO/MURI under Grant W911NF-04-1-0170 and from the NASA University Research, Engineering, and Technology Institute on BioInspired Materials (BIMat) under Award No. NCC-1-02037 is greatly appreciated.

References and Notes

(1) von Rybinski, W.; Schwuger, M. J. *Langmuir* **1986**, *2*, 639−643.
(2) Vakarelski, I. U.; Brown, S. C.; Rabinovich, Y. I.; Moudgil, B. M. *Langmuir* **2004**, *20*, 1724−1731.
(3) Sulek, M. W.; Wasilewski, T. *Wear* **2006**, *260*, 193−204.
(4) Hills, B. A. *Proc. Inst. Mech. Eng., Part H* **2000**, *214*, 83−94.
(5) Subramanian, V.; Ducker, W. A. *Langmuir* **2000**, *16*, 4447−4454.
(6) Russel, W. B.; Saville, D. A.; Schowalter, W. R. *Colloidal Dispersions*; Cambridge University Press: New York, 1989.
(7) Gong, X.; Liu, J.; Baskaran, S.; Voise, R. D.; Young, J. S. *Chem. Mater.* **2000**, *12*, 1049−1052.
(8) Kar, G.; Fuerstenau, D. W. *J. Electrochem. Soc.* **1972**, *119*, 33−39.
(9) Wei, Z.; Somasundaran, P.; Duby, P. *J. Electrochem. Soc.* **2004**, *151*, B304−B308.
(10) Harfenist, S. A.; Wang, Z. L.; Alvarez, M. M.; Vezmar, I.; Whetten, R. L. *J Phys. Chem.* **1996**, *100*, 13904−13910.
(11) Manna, L.; Scher, E. C.; Alivisatos, A. P. *J. Am. Chem. Soc.* **2000**, *122*, 12700−12706.
(12) Nikoobakht, B.; El-Sayed, M. A. *Chem. Mater.* **2003**, *15*, 1957−1962.
(13) Sivaraja, S. R.; Zettlemoyer, A. C.; Narayan, K. S. *J. Phys. Chem.* **1963**, *67*, 2112−2113.
(14) Kipling, J. J., *Adsorption from Solutions of Non-electrolytes*, U.S. Ed.; Academic Press: London, 1965.
(15) Groszek, A. J. *Proc. R. Soc. London, Ser. A* **1970**, *314*, 473−498.
(16) Somasundaran, P.; Fuerstenau, D. W. *J. Phys. Chem.* **1966**, *70*, 90−96.
(17) Benton, D. P.; Sparks, B. D. *Trans. Faraday Soc.* **1966**, *62*, 3244−3252.
(18) Benton, D. P.; Sparks, B. D. *Trans. Faraday Soc.* **1967**, *63*, 2270−2274.
(19) Gaudin, A. M.; Fuerstenau, D. W. *Trans. AIME* **1955**, *202*, 958−962.
(20) Tiberg, F.; Jönsson, B.; Lindman, B. *Langmuir* **1994**, *10*, 3714−3722.

(21) Tiberg, F. *J. Chem. Soc., Faraday Trans.* **1996**, *92*, 531−538.
(22) Besio, G. J.; Prud'homme, R. K.; Benziger, J. B. *Langmuir* **1988**, *4*, 140−144.
(23) Pagac, E. S.; Prieve, D. C.; Tilton, R. D. *Langmuir* **1998**, *14*, 2333−2342.
(24) Atkin, R.; Craig, V. S. J.; Biggs, S. *Langmuir* **2001**, *17*, 6155−6163.
(25) Okahata, Y.; Ebato, H. *Anal. Chem.* **1991**, *63*, 203−207.
(26) Clark, S. C.; Ducker, W. A. *J. Phys. Chem. B* **2003**, *107*, 9011−9021.
(27) Chandar, P.; Somasundaran, P. *J. Colloid Interface Sci.* **1987**, *117*, 31−46.
(28) McDermott, D. C.; McCamey, J.; Thomas, R. K.; Rennie, A. R. *J. Colloid Interface Sci.* **1994**, *162*, 304−310.
(29) Steitz, R.; Müller-Buschbaum, P.; Schemmel, S.; Cubitt, R.; Findenegg, G. H. *Europhys. Lett.* **2004**, *67*, 962−968.
(30) Drach, M.; Narkiewicz-Michałek, J.; Rudzinski, W.; Findenegg, G. H.; Király, Z. *Phys. Chem. Chem. Phys.* **2002**, *4*, 2307−2319.
(31) Király, Z.; Findenegg, G. H. *Langmuir* **2000**, *16*, 8842−8849.
(32) Király, Z.; Findenegg, G. H. *Langmuir* **2005**, *21*, 5047−5054.
(33) Király, Z.; Findenegg, G. H. *J. Phys. Chem. B* **1998**, *102*, 1203−1211.
(34) Király, Z.; Findenegg, G. H.; Mastalir, Á. *Langmuir* **2006**, *22*, 3207−3213.
(35) Manne, S.; Cleveland, J. P.; Gaub, H. E.; Stucky, G. D.; Hansma, P. K. *Langmuir* **1994**, *10*, 4409−4413.
(36) Manne, S.; Gaub, H. E. *Science* **1995**, *270*, 1480−1482.
(37) Ducker, W. A.; Wanless, E. J. *Langmuir* **1996**, *12*, 5915−5920.
(38) Wanless, E. J.; Ducker, W. A. *J. Phys. Chem.* **1996**, *100*, 3207−3214.
(39) Wolgemuth, J. L.; Workman, R. K.; Manne, S. *Langmuir* **2000**, *16*, 3077−3081.
(40) Lamont, R. E.; Ducker, W. A., *J. Am. Chem. Soc.* **1998**, *120*, 7602−7607.
(41) Shah, K.; Chiu, P.; Sinnott, S. B. *J. Colloid Interface Sci.* **2005**, *296*, 342−349.
(42) Manne, S.; Schäffer, T. E.; Huo, Q.; Hansma, P. K.; Morse, D. E.; Stucky, G. D.; Aksay, I. A. *Langmuir* **1997**, *13*, 6382−6387.
(43) Saville, D. A.; Chun, J.; Li, J.-L.; Schniepp, H. C.; Car, R.; Aksay, I. A. *Phys. Rev. Lett.* **2006**, *96*, 018301.
(44) Schniepp, H. C.; Saville, D. A.; Aksay, I. A. *J. Am. Chem. Soc.* **2006**, *128*, 12378−12379.
(45) Wanless, E. J.; Ducker, W. A. *Langmuir* **1997**, *13*, 1463−1474.
(46) Velegol, S. B.; Fleming, B. D.; Biggs, S.; Wanless, E. J.; Tilton, R. D. *Langmuir* **2000**, *16*, 2548−2556.
(47) Schulz, J. C.; Warr, G. G. *Langmuir* **2002**, *18*, 3191−3197.
(48) Ducker, W. A.; Grant, L. M. *J. Phys. Chem.* **1996**, *100*, 11507−11511.
(49) Liu, J.-F.; Ducker, W. A. *J. Phys. Chem. B* **1999**, *103*, 8558−8567.
(50) Petrov, I.; Barna, P. B.; Hultman, L.; Greene, J. E. *J. Vac. Sci. Technol., A* **2003**, *21*, S117−S128.
(51) Wanless, E. J.; Davey, T. W.; Ducker, W. A. *Langmuir* **1997**, *13*, 4223−4228.
(52) Mysels, K. J. *Langmuir* **1986**, *2*, 423−428.
(53) Hayashi, S.; Ikeda, S. *J. Phys. Chem.* **1980**, *84*, 744−751.
(54) Jaschke, M.; Butt, H.-J.; Gaub, H. E.; Manne, S. *Langmuir* **1997**, *13*, 1381−1384.
(55) Burgess, I.; Jeffrey, C. A.; Cai, X.; Szymanski, G.; Galus, Z.; Lipkowski, J. *Langmuir* **1999**, *15*, 2607−2616.
(56) Chidsey, C. E. D.; Loiacono, D. N.; Sleator, T.; Nakahara, S. *Surf. Sci.* **1988**, *200*, 45−66.
(57) Gray, A. *Modern differential geometry of curves and surfaces with Mathematica;* CRC Press: Boca Raton, FL, 1998.
(58) Senden, T. J.; Drummond, C. J.; Kekicheff, P. *Langmuir* **1994**, *10*, 358−362.
(59) Patrick, H. N.; Warr, G. G.; Manne, S.; Aksay, I. A. *Langmuir* **1997**, *13*, 4349−4356.
(60) Albrecht, T. R.; Akamine, S.; Carver, T. E.; Quate, C. F. *J. Vac. Sci. Technol., A* **1990**, *8*, 3386−3396.
(61) Vaknin, D.; Dahlke, S.; Travesset, A.; Nizri, G.; Magdassi, S. *Phys. Rev. Lett.* **2004**, *93*, 218302.
(62) Bousse, L. J.; Mostarshed, S.; Hafeman, D. *Sens. Actuators, B* **1992**, *10*, 67−71.